© 2019. Published by The Company of Biologists Ltd | Journal of Cell Science (2019) 132, jcs225029. doi:10.1242/jcs.225029

RESEARCH ARTICLE

MYO1C stabilizes actin and facilitates the arrival of transport carriers at the Golgi complex

Anahi Capmany[1,2], Azumi Yoshimura[1,2], Rachid Kerdous[1,2], Valentina Caorsi[3], Aurianne Lescure[1,4], Elaine Del Nery[1,4], Evelyne Coudrier[1,2], Bruno Goud[1,2] and Kristine Schauer[1,2,*]

ABSTRACT

In this study, we aimed to identify the myosin motor proteins that control trafficking at the Golgi complex. In addition to the known Golgi-associated myosins MYO6, MYO18A and MYH9 (myosin IIA), we identified MYO1C as a novel player at the Golgi in a human cell line. We demonstrate that depletion of *MYO1C* induces Golgi complex fragmentation and decompaction. MYO1C accumulates at dynamic structures around the Golgi complex that colocalize with Golgi-associated actin dots. *MYO1C* depletion leads to loss of cellular F-actin, and Golgi complex decompaction is also observed after inhibition or loss of the actin-related protein 2/3 complex, Arp2/3 (also known as ARPC). We show that the functional consequence of *MYO1C* depletion is a delay in the arrival of incoming transport carriers, both from the anterograde and retrograde routes. We propose that MYO1C stabilizes actin at the Golgi complex, facilitating the arrival of incoming transport carriers at the Golgi.

This article has an associated First Person interview with the first author of the paper.

KEY WORDS: Arp2/3, Golgi apparatus, Myosin1, Pleckstrin hology domain, Rab11, Rab6, MYO6, MYO18A, MYH9, Myosin IIA

INTRODUCTION

The Golgi complex is the main hub of intracellular trafficking, at the interface between anterograde and retrograde routes. Golgi membrane dynamics are mandatory for efficient sorting of cargos traversing the Golgi complex and require tensile forces from the cytoskeleton. Particularly, actin-dependent myosin motor proteins have been implicated in the formation of tubular membrane carriers and their fission from the Golgi: historically, non-muscle myosin IIA (MYH9) was first proposed to function in the production of vesicles from the Golgi complex (Müsch et al., 1997). More recently, the depletion and inhibition of myosin II induced the appearance of long, Golgi-derived, Rab6 (also known as Rab6a)-positive membrane tubules, further supporting its role in fission events during *trans*-Golgi network (TGN) exit (Miserey-Lenkei et al., 2010). Myosin VI family member MYO6, a myosin moving towards the minus ends of F-actin, has also been found on Golgi membranes, and was shown to play a role in Golgi ribbon formation and exocytic events (Warner et al., 2003). Moreover, MYO18A, MYO1B and MYO5B were additionally proposed to control the formation of tubular and vesicular membrane carriers from Golgi and TGN membranes (Dippold et al., 2010; Almeida et al., 2011; Liu et al., 2013). Interestingly, although Golgi-associated myosins belong to different classes, they all have been proposed to facilitate exit from the Golgi complex. Here, we aimed to systematically analyze the myosins that regulate trafficking at the Golgi level, and to characterize the underlying molecular mechanisms by which they regulate Golgi membrane dynamics.

RESULTS

Identification of myosins that alter Golgi morphology

Defects in Golgi trafficking are characterized by changes in Golgi morphology (Goud et al., 2018). Thus, we systematically depleted 36 myosins present in human and sought those that altered Golgi morphology. We employed our approach combining cell culture on adhesive micropatterns and quantification of organelle positioning by probabilistic density mapping (Schauer et al., 2010, 2014; Duong et al., 2012). We have previously shown that, when seeded on micropatterns, the Golgi complex has a characteristic, well-defined, stable and reproducible position, allowing automated detection of subtle changes in its organization in a reduced number of cells (Schauer et al., 2010). In three independent experiments, human telomerase-immortalized retinal pigmented epithelial (hTertRPE-1) cells were transfected with a small interfering RNA (siRNA) library targeting each myosin with four independent siRNAs (Fig. 1A). The Golgi complex was analyzed in fixed, crossbow-shaped micropatterned cells using our density-based statistical analysis as previously reported (Duong et al., 2012; Schauer et al., 2014). Hits were established by comparing each siRNA-treated well with six control wells. We selected myosins for further analysis if average Golgi morphology of a siRNA-treated well was significantly different to those of three independent control wells (50% of control), and reproducible for one specific siRNA in three independent experiments (Fig. 1B, red dots) or for two siRNAs in two independent experiments (Fig. 1B, orange dots). This was the case for 17 myosins (~50%) from seven different classes. We next tested the expression level of the identified myosins in hTertRPE-1 cells (Fig. 1C). Class II skeletal and cardiac muscle myosins, expected not to be expressed in hTertRPE-1 cells, were expressed at the detection limit as judged by analysis of *MYH6* and *MYH15* (Fig. 1C, note the logarithmic representation). We suspect that the presence of these hits is due to off-target effects of the siRNAs and speculate that the absence of a target for those siRNAs could be the reason why they exert strong effects on Golgi morphology. Similarly, the expression levels of *MYO3A*, *MYO10*, *MYO15A* and *MYH11* were at the detection limit, rendering a further analysis very challenging. However, the mRNA level of *MYH9*, *MYO1C*, *MYO18A* and *MYO6* was significant (expression >0.1% of GAPDH level). Probability density maps of the Golgi complex of pooled cells from significant wells revealed that gene silencing of

[1]Institut Curie, PSL Research University, Molecular Mechanisms of Intracellular Transport group, 75248 Paris, France. [2]Centre National de la Recherche Scientifique, Unité Mixte de Recherche 144, 75005 Paris, France. [3]Abbelight, 75005 Paris, France. [4]Department of Translational Research, BioPhenics High-Content Screening Laboratory, Cell and Tissue Imaging Facility (PICT-IBiSA), 75005 Paris, France.

*Author for correspondence (kristine.schauer@curie.fr)

V.C., 0000-0003-4166-9600; E.C., 0000-0001-6011-8922; B.G., 0000-0003-1227-4159; K.S., 0000-0002-6102-8790

Received 11 September 2018; Accepted 1 March 2019

Journal of Cell Science (2019) 132, jcs225029. doi:10.1242/jcs.225029

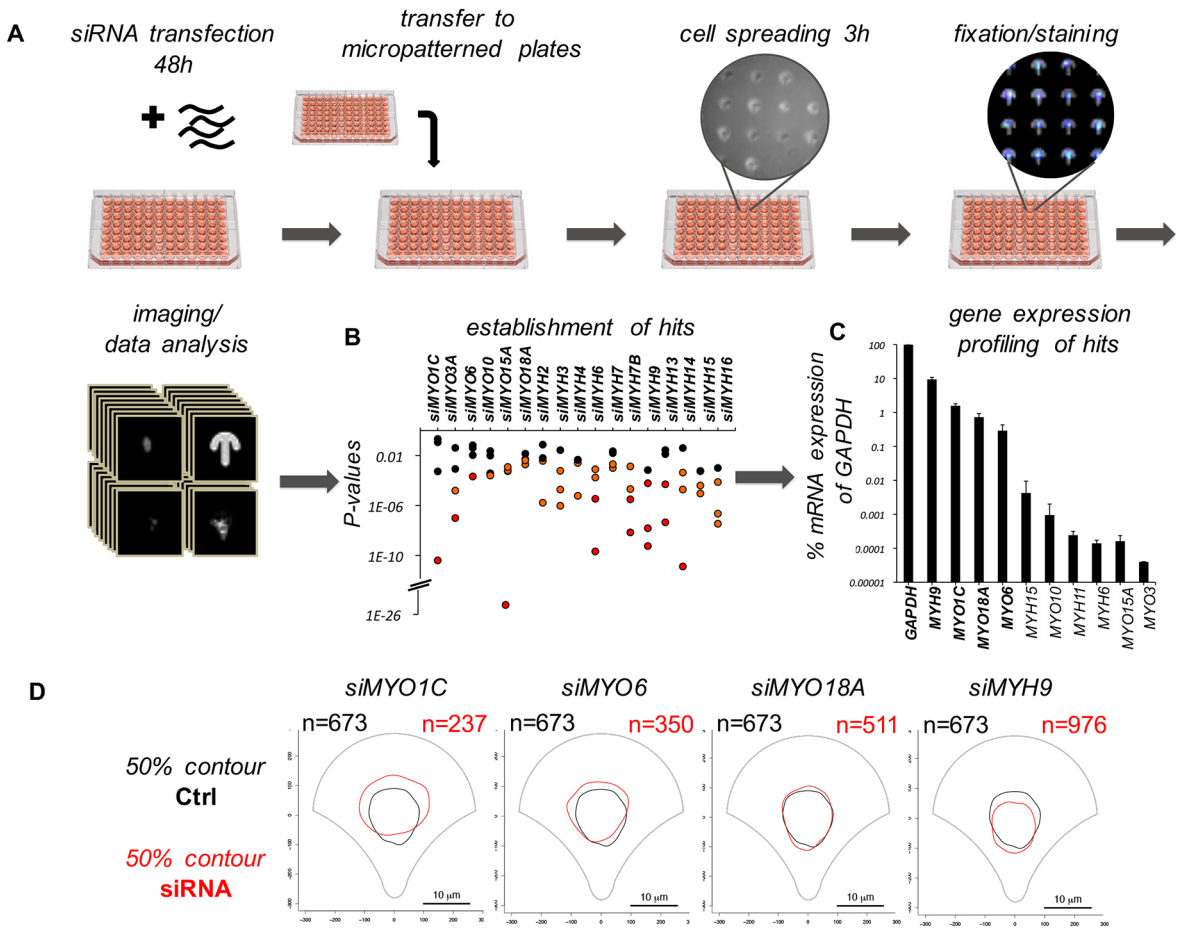

Fig. 1. Identification of myosins that alter Golgi morphology. (A) Workflow for the systematic, comparative analysis, combining cell culture on adhesive micropatterns and quantification of organelle positioning by probabilistic density mapping: hTertRPE-1 cells were transfected with an siRNA library targeting each myosin with four independent siRNAs, incubated for 48 h and transferred to crossbow-shaped micropatterned plates. After 3 h spreading, cells were fixed, and the Golgi complex was stained with anti-GM130 antibody and imaged, followed by image processing and density-based statistical analysis. (B) A list of candidate myosins that were further investigated was established on the following criteria: average density map of the Golgi complex was significantly different to those of three independent control wells, and reproducible for one specific siRNA in three independent experiments (red dots) or for two siRNAs in two independent experiments (orange dots). Black dots represent not significant hits. (C) The expression level of the identified myosins (excluding members of skeletal and cardiac muscle myosins) in hTertRPE-1 cells as a percentage of GAPDH expression. Error bars represent the s.d. of three independent measurements. (D) Overlap of the 50% contour of the 2D density estimation map calculated in control cells (black) or cells depleted of the indicated myosin (red), *n*=number of analyzed cells.

MYO1C, *MYO6* and *MYO18* increased the area in which Golgi structures were found compared to that in pooled control cells (Fig. 1D). However, gene silencing of *MYH9* decreased the area of the 50% Golgi complex probability contour (Fig. 1D). MYH9, MYO18A and MYO6 have been all reported to regulate trafficking at the Golgi level (Dippold et al., 2010; Müsch et al., 1997; Miserey-Lenkei et al., 2010; Warner et al., 2003), validating our density-based analysis. To verify that *MYO1C* depletion affects Golgi morphology, we tested all four siRNAs used in the screen. We found that all four siRNAs reduced expression levels of MYO1C under screen conditions (2 days of knockdown), however only by 25–40% (Fig. S1A,B). We found that all four siRNAs affected Golgi complex morphology, although not with the same efficiency (Fig. S1C–E); the siRNA#3, identified under screen conditions, showed the strongest phenotype. Thus, our analysis identified MYO1C as a potential novel regulator at the Golgi complex.

Comparable analysis of Golgi morphology upon depletion of different myosins

To further verify and characterize the identified myosins, we analyzed the 3D cellular phenotypes for individual siRNAs (Fig. 2). We used siRNA#1, which showed an intermediate phenotype under screen conditions, to target *MYO1C* for all further studies. The gene expression of all identified myosins was reduced by 60–90% after 3 days of siRNA-induced gene silencing (Fig. S2A). Representative images of single cells (Fig. 2A) and the volume of the 3D density maps of ∼100 cells from three independent experiments confirmed that gene silencing of *MYO1C*, *MYO6* and *MYO18* increased the area in which Golgi structures were found, compared to that in pooled control cells, whereas gene silencing of *MYH9* slightly decreased this area (Fig. 2B,C). Moreover, automated detection of individual Golgi structures in single cells revealed that depletion of *MYO1C* and *MYO18A* significantly increased the average number of detectable Golgi structures per cell, indicating Golgi complex fragmentation (Fig. 2D). Depletion of *MYH9* significantly decreased the average number of Golgi structures per cell. Dividing the average numbers of structures per cell by the average volume of the 3D density map indicated that depletion of *MYO1C* and *MYO6* de-compacted the Golgi complex by 40% and 25%, respectively. Depletion of *MYO18A* led to a 50% compaction of this organelle, whereas gene silencing of *MYH9* did not change

Journal of Cell Science (2019) 132, jcs225029. doi:10.1242/jcs.225029

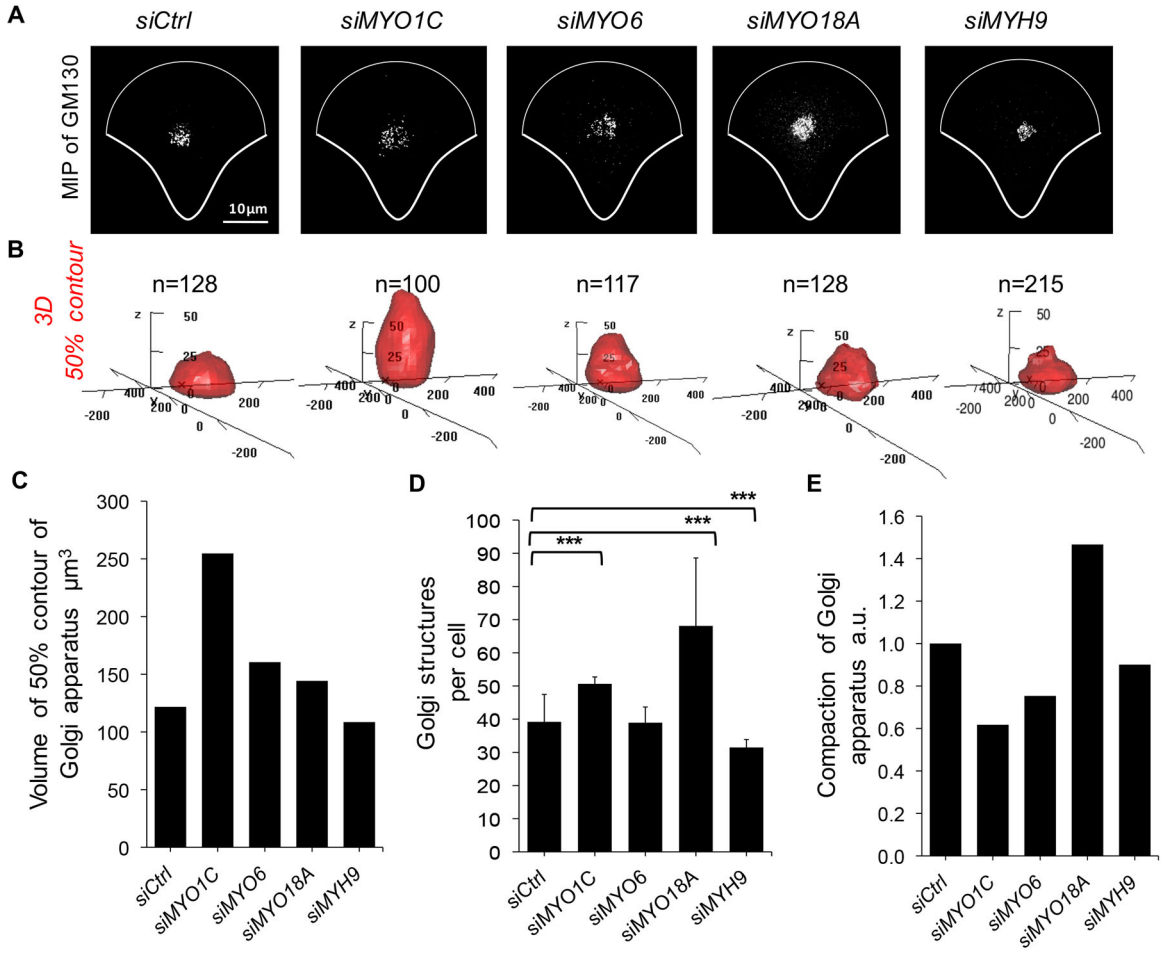

Fig. 2. Comparable analysis of Golgi morphology upon depletion of different myosins. (A) Fluorescent images representing the maximum intensity projections (MIPs) of the Golgi complex labeled by anti-GM130 in single, representative hTertRPE-1 cells depleted of the indicated myosin and seeded on a crossbow-shaped micropattern. Scale bar: 10 µm. (B) 3D 50% density map of the Golgi complex as in A. *n*=number of analyzed cells. Axes are in pixels, 100 pixels=6.45 µm. (C) Volume of the 50% contour of the Golgi complex as in B. (D) Quantification of the average numbers of Golgi structures per cell as in B. Error bars represent the s.d. of three independent experiments. ***$P<1\times10^{-4}$, Student's *t*-test. (E) Quantification of the compaction of the Golgi complex, dividing the average number of Golgi structures per cell by the volume of the 50% probability contour.

compaction of the Golgi complex to more than 10% (Fig. 2D). Thus, our results indicate that *MYO1C* and *MYO6* depletion de-compacts the Golgi complex, whereas depletion of *MYO18A* and *MYH9* leads to a more compact or smaller Golgi complex, increasing the number of Golgi structures in the case of *MYO18A* silencing, and decreasing the Golgi area and number of Golgi structures downstream of *MYH9* depletion.

MYO1C controls Golgi morphology

We next studied the function of MYO1C at the Golgi (employing siRNA#1, see Fig. S1). As expected from mRNA levels, the MYO1C protein level was reduced by 80% after 3 days of siRNA treatment (Fig. S2B,C). Analysis of the Golgi morphology in classical, unconstrained cell culture conditions confirmed that the Golgi complex was fragmented and the 2D projected Golgi area was significantly increased upon *MYO1C* depletion (Fig. 3A,B). Notably, all tested Golgi markers, the matrix protein GM130 (also known as GOLGA2), the *cis*-Golgi protein Giantin (also known as GOLGB1) and the TGN protein TGN46 (also known as TGOLN2), exhibited altered morphology. Rescue experiments through the transient overexpression of a GFP-MYO1C construct (of the rat homolog) that is resistant against knockdown by the siRNA used in this study failed in hTertRPE-1 cells because of cell death after transfection. Thus, we performed rescue experiments in previously characterized stable HeLa cell lines that express either GFP-tagged human MYO1C or mouse MYO1C (Maliga et al., 2013). Gene silencing of *MYO1C* strongly decreased expression of the endogenous MYO1C in all HeLa cells, as well as the overexpressed human GFP-MYO1C but not the mouse GFP-MYO1C (Fig. S2D,E). As expected, the Golgi complex expanded after siRNA treatment of HeLa cells expressing the human protein, but not in HeLa cells expressing the mouse isoform (Fig. S2F). Because HeLa cells show a more heterogeneous morphology of the Golgi, the 75% probability contour representing 75% of all Golgi structures was plotted. We also noticed that the Golgi seems to be slightly smaller after siRNA treatment in HeLa cells expressing the mouse MYO1C. In hTertRPE1 cells, the overexpression of a GFP-MYO1C construct (of the rat homolog) led to a significant compaction of the Golgi complex that was not detected after the expression of GFP alone (Fig. 3C,D). To study Golgi complex alterations at the ultrastructural level, we examined the MYO1C-depleted cells using electron microscopy (EM). EM showed that the characteristic structure of Golgi stacks, comprising four to six cisternae with a typical *cis-trans* Golgi and endoplasmic reticulum (ER) membrane, was similar in *MYO1C*-depleted cells and control cells. Although the Golgi appeared less compact, EM confirmed that the Golgi complex was dispersed and not swollen (Fig. 3E).

Journal of Cell Science (2019) 132, jcs225029. doi:10.1242/jcs.225029

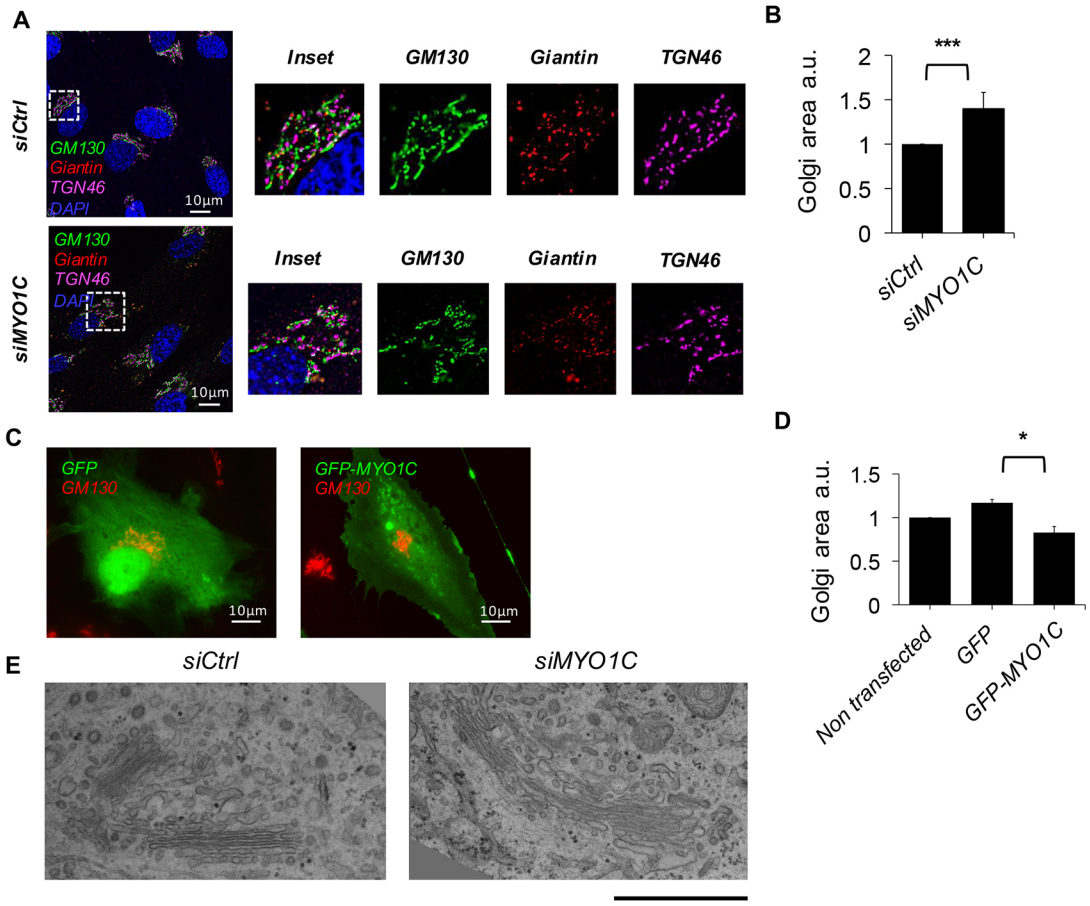

Fig. 3. MYO1C controls Golgi morphology. (A) Immunofluorescent staining of different Golgi markers – the matrix protein GM130 (green), the *cis*-Golgi protein Giantin (red) and the TGN protein TGN46 (magenta) – in representative control (top) and MYO1C-depleted (bottom) hTertRPE-1 cells in classical, unconstrained culture conditions. Nuclei are stained with DAPI (blue). Scale bars: 10 µm. (B) Quantification of the 2D projected Golgi area in control conditions (n=145) and upon *MYO1C* depletion (n=165). Error bars represent the s.d. of three independent experiments; n=number of analyzed cells. ***$P<1\times10^{-4}$, Student's t-test. (C) Fluorescent images of representative hTertRPE-1 cells expressing GFP or GFP-MYO1C (green) and stained for the Golgi complex (red, GM130). Scale bars: 10 µm. (D) Quantification of the 2D projected Golgi area (stained by GM130) of non-transfected cells and cells as in C. Error bars represent the s.d. of three independent experiments with n>40 cells for each condition. *$P<1\times10^{-2}$, Student's t-test, average of three independent experiments. (E) EM images of representative intracellular areas of unconstrained hTertRPE-1 cells containing the Golgi complex in control conditions (left) and upon *MYO1C* depletion (right). Scale bar: 1 µm.

MYO1C accumulates at the Golgi proximity by pleckstrin homology domain and colocalizes with actin spots

We next investigated the cellular localization of MYO1C. Immunofluorescent staining of endogenous MYO1C or overexpression of GFP-MYO1C indicated that the majority of MYO1C was at the plasma membrane, as expected (Ruppert et al., 1995). However, in addition to this major pool, we identified MYO1C-containing spots in close apposition to the Golgi complex (Fig. 4A–C; Fig. S3A). Overexpressed GFP-MYO1C showed similar distribution to the endogenous protein, as quantified by average intensity projections of fluorescent images and density maps of endogenous and overexpressed MYO1C in micropatterned cells, and the average expression of GFP-MYO1C protein was comparable to endogenous levels (Fig. S3B–D). Previous analysis has identified recycling endosomes that are found close to the Golgi complex as an additional intracellular localization of MYO1C (Brandstaetter et al., 2012). Thus, we performed colocalization analysis of endogenous and overexpressed GFP-MYO1C with different markers of intracellular compartments: the TGN protein TGN46, the recycling endosome-specific Rab11 (also known as Rab11a) GTPase, the late endosomal/lysosomal protein Lamp1 and the early endosomal marker EEA1 (Fig. S4). Additionally, we used the colocalization between MYO1C and actin visualized by Ftractin (Johnson and Schell, 2009) as a positive control, showing strong colocalization. Colocalization analysis was performed in several tens of cells using an object-based method, in which two structures were considered colocalized if the distance between their centroids was found to be inferior to the optical resolution limit. We found that, on average, 18% and 19% of endogenous or overexpressed MYO1C colocalized with TGN46 and Rab11, respectively (Fig. 4D; see Fig. S4C for individual experiments). The colocalization with other endosomal markers was less: we found 10% and 6% colocalization with late endosomes and early endosomes, respectively. Thus, our analysis indicates that a significant intracellular MYO1C pool is found on recycling endosomes and late endosomes, as previously reported, as well as on the TGN.

Live-cell imaging of GFP-MYO1C revealed that MYO1C-positive structures moved around the Golgi complex (Fig. 4E; Movie 1). Moreover, we found that both endogenous MYO1C and GFP-MYO1C colocalized with actin spots at the Golgi (Fig. 5A,B). To verify that the recruitment of MYO1C in the proximity of the Golgi complex was independent of its actin-dependent motor activity, as previously reported (Tang and Ostap, 2001; Pyrpassopoulos et al., 2012), we compared accumulation of the

Journal of Cell Science (2019) 132, jcs225029. doi:10.1242/jcs.225029

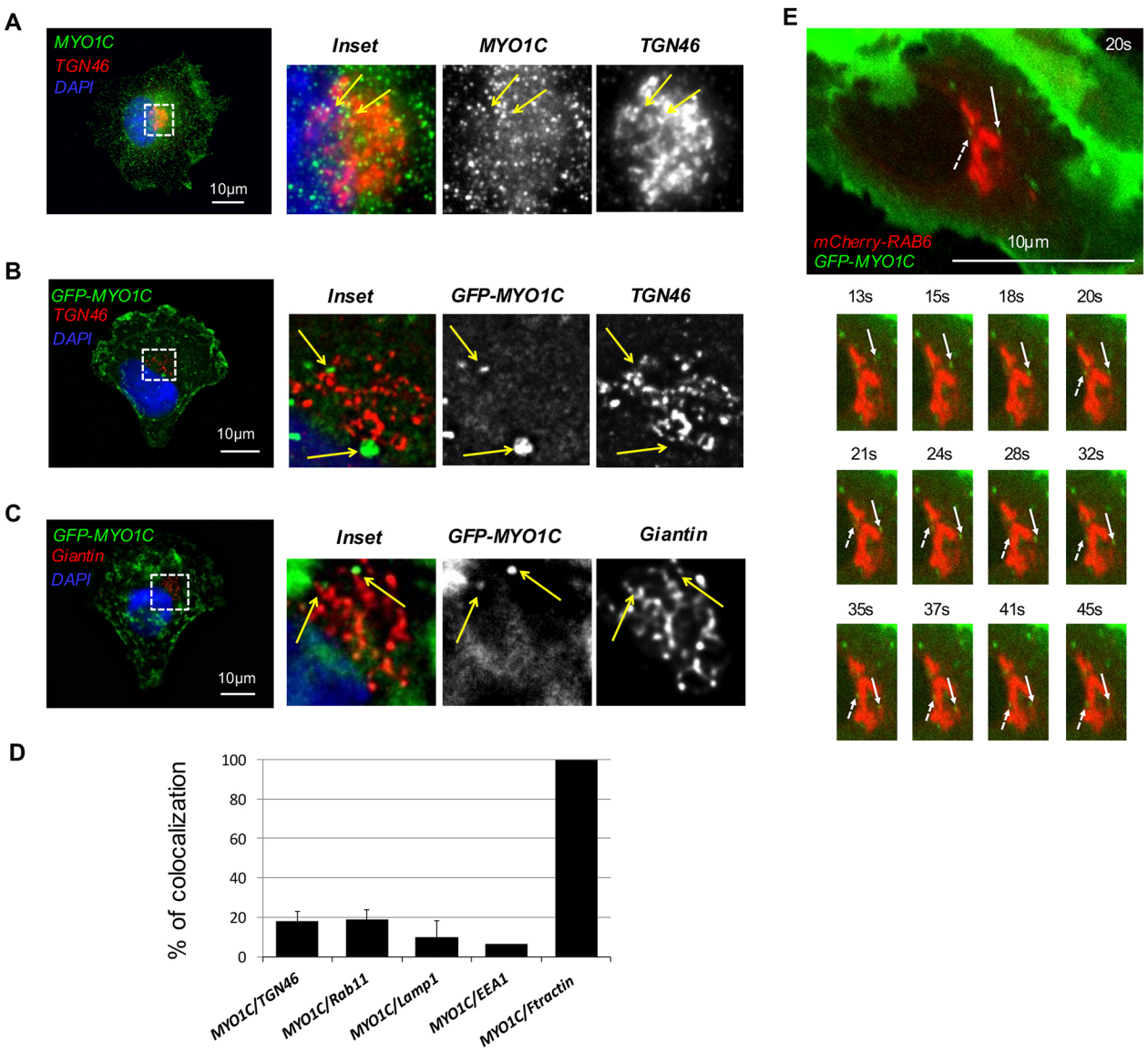

Fig. 4. MYO1C accumulates at the Golgi proximity. (A) Fluorescent images of a representative, unconstrained hTertRPE-1 cell stained with anti-MYO1C antibody to visualize the endogenous protein (green), anti-TGN46 antibody to visualize the Golgi complex (red) and DAPI to visualize the nucleus (blue). (B,C) Fluorescent images of representative, micropatterned hTertRPE-1 cells expressing GFP-MYO1C (green), and stained for the Golgi complex with anti-TGN46 or anti-Giantin antibody (red) and for the nucleus with DAPI (blue). Yellow arrows indicate MYO1C-positive structures at the Golgi complex proximity. (D) Colocalization analysis of endogenous or overexpressed GFP-MYO1C with the following markers: anti-TGN46 (TGN), Rab11 (recycling endosomes), Lamp1 (late endosomes/lysosomes), EEA1 (early endosomes) and Ftractin (actin cytoskeleton). Colocalization analysis was performed using an object-based method, in which two structures were considered colocalized if the distance between their centroids (from automated segmentation) was inferior to the optical resolution limit (350 nm X-Y, 900 nm Z). Colocalization results are given as the percentage of colocalized structures over the total numbers of MYO1C-positive structures. Error bars represent the s.d. of four independent experiments for TGN46, three independent experiments for Rab11 and two independent experiments for Lamp1. The individual experiments with analyzed cell numbers are shown in Fig. S4. (E) Fluorescent images of a time-lapse acquisition of unconstrained hTertRPE-1 cells expressing GFP-MYO1C (green) and mCherry-Rab6 (red). Scale bars: 10 µm. White solid and dashed arrows indicate two independent MYO1C-positive structures moving around the Golgi complex.

overexpressed GFP-MYO1C with that of an actin-binding mutant GFP-MYO1CΔABL (Joensuu et al., 2014), in which the myopathy loop (323–330; IIAKGEEL) was replaced by AGA tripeptide, disrupting the essential hydrophobic interactions between the myosin head domain and actin filaments (Fig. 5C). Additionally, we analyzed the accumulation of a truncated construct (GFP-Tail) containing only the MYO1C lipid-binding pleckstrin homology (PH) domain (Hokanson et al., 2006; Oh et al., 2013). We found that GFP-MYO1CΔABL formed the same numbers of spots at the Golgi as the non-mutated GFP-MYO1C, indicating that accumulation of MYO1C in the proximity of the Golgi complex (marked by GM130) is independent of its actin-dependent motor activity (Fig. 5D,E). Overexpression of the GFP-Tail increased the presence of Golgi-associated spots, indicating that the PH domain is responsible for accumulation around the Golgi. Interestingly, the expression of either GFP-MYO1CΔABL or the GFP-Tail did not change Golgi complex area (Fig. S3E), indicating that both constructs did not show dominant-negative effects in hTertRPE1 cells. Together, these results indicate that MYO1C accumulates in the proximity of the Golgi complex by its PH domain and that

Journal of Cell Science (2019) 132, jcs225029. doi:10.1242/jcs.225029

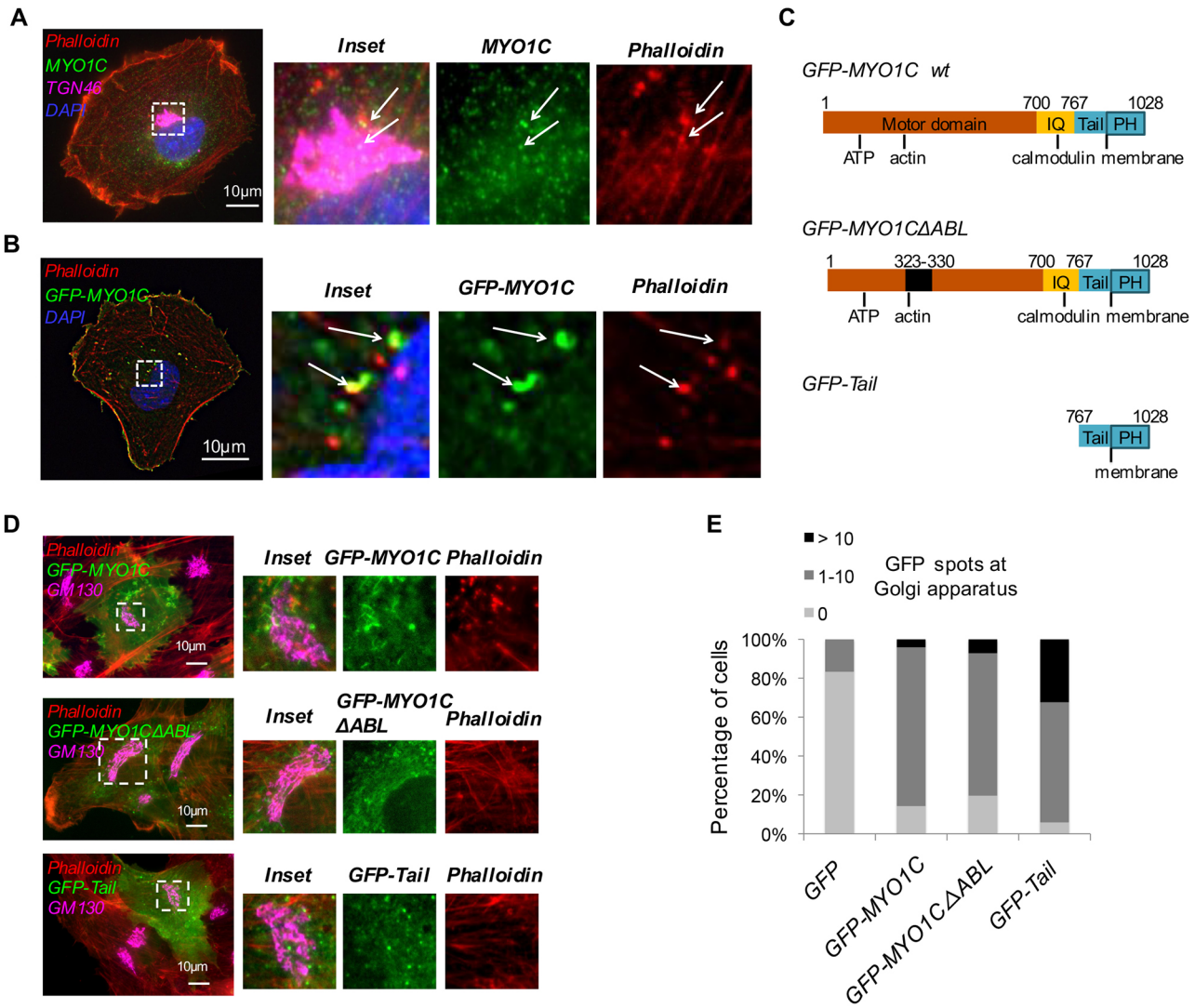

Fig. 5. MYO1C colocalizes with actin at the Golgi proximity but its recruitment is independent of its actin-binding domain. (A) Fluorescent images of a representative, unconstrained hTertRPE-1 cell stained with anti-MYO1C antibody to visualize the endogenous protein (green), TGN46 antibody to visualize the Golgi complex (magenta) and phalloidin to visualize the actin cytoskeleton (red). The nucleus is stained with DAPI (blue). (B) Fluorescent images of representative, micropatterned hTertRPE-1 cells expressing GFP-MYO1C (green), and stained with phalloidin to visualize F-actin (red) and DAPI to visualize the nucleus (blue). Arrows indicate MYO1C-positive structures that colocalize with Golgi-associated actin spots. (C) Domain structure of MYO1C, the mutant form MYO1CΔABL and the truncated Tail domain. (D) Fluorescent images of representative hTertRPE-1 cells expressing GFP-MYO1C, GFP-MYO1CΔABL or GFP-Tail (green), stained for the Golgi complex (magenta, GM130) and F-actin (red, phalloidin). (E) Quantification of GFP-positive spots at the Golgi area as in D for GFP (n=24), GFP-MYO1C (n=49), GFP-MYO1CΔABL (n=56) or GFP-Tail (n=34). The percentage of cells that contain 0 (light gray), 1–10 (dark gray) or more than 10 (black) Golgi-associated spots per cell is shown. Note that control (GFP-expressing) cells never contained more than one Golgi-associated spot per cell. n=number of analyzed cells. Scale bars: 10 µm.

interaction of MYO1C with actin is important for Golgi morphology changes.

MYO1C controls the cellular actin cytoskeleton

Next, we investigated the organization of the actin cytoskeleton in the presence and absence of MYO1C, employing micropatterned, normalized cells for better comparison. Although actin protein levels were not changed upon *MYO1C* depletion (Fig. 6A), staining of F-actin with phalloidin in normalized cells revealed a decrease in actin fibers throughout the cell upon *MYO1C* depletion (Fig. 6B). This suggested that MYO1C stabilizes F-actin. Thus, we wondered whether actin depolymerization by different drugs could mimic *MYO1C* depletion. We treated cells with Latrunculin A (LatA), to disrupt actin filaments (200 nM for 20 min), and CK666, an inhibitor of the Arp2/3 (also known as ACTR2/3) complex, to inhibit branched actin formation (100 µM for 20 min), and observed the Golgi complex in hTertRPE-1 cells stably expressing the Golgi marker GFP-Rab6 (Fig. 6C). Whereas LatA treatment did not increase Golgi complex area, the loss of branched actin after inhibition of the Arp2/3 complex by CK666 significantly increased the Golgi complex area (Fig. 6D). Similarly, targeting ACTR3 of the Arp2/3 complex by siRNA resulted in a fragmented Golgi and an increase in Golgi area compared to that of control in micropatterned cells (Fig. 6E,F). These results indicate that *MYO1C* depletion mimics loss of branched actin. To further investigate the interaction of MYO1C with the actin cytoskeleton, we performed super-resolution microscopy based on single-molecule localization of MYO1C and phalloidin-stained actin. Interestingly, we observed that MYO1C is frequently found at branched actin filaments (Fig. S5). Based on our results, we speculate that MYO1C stabilizes branched actin close to cellular membranes including the Golgi complex.

Journal of Cell Science (2019) 132, jcs225029. doi:10.1242/jcs.225029

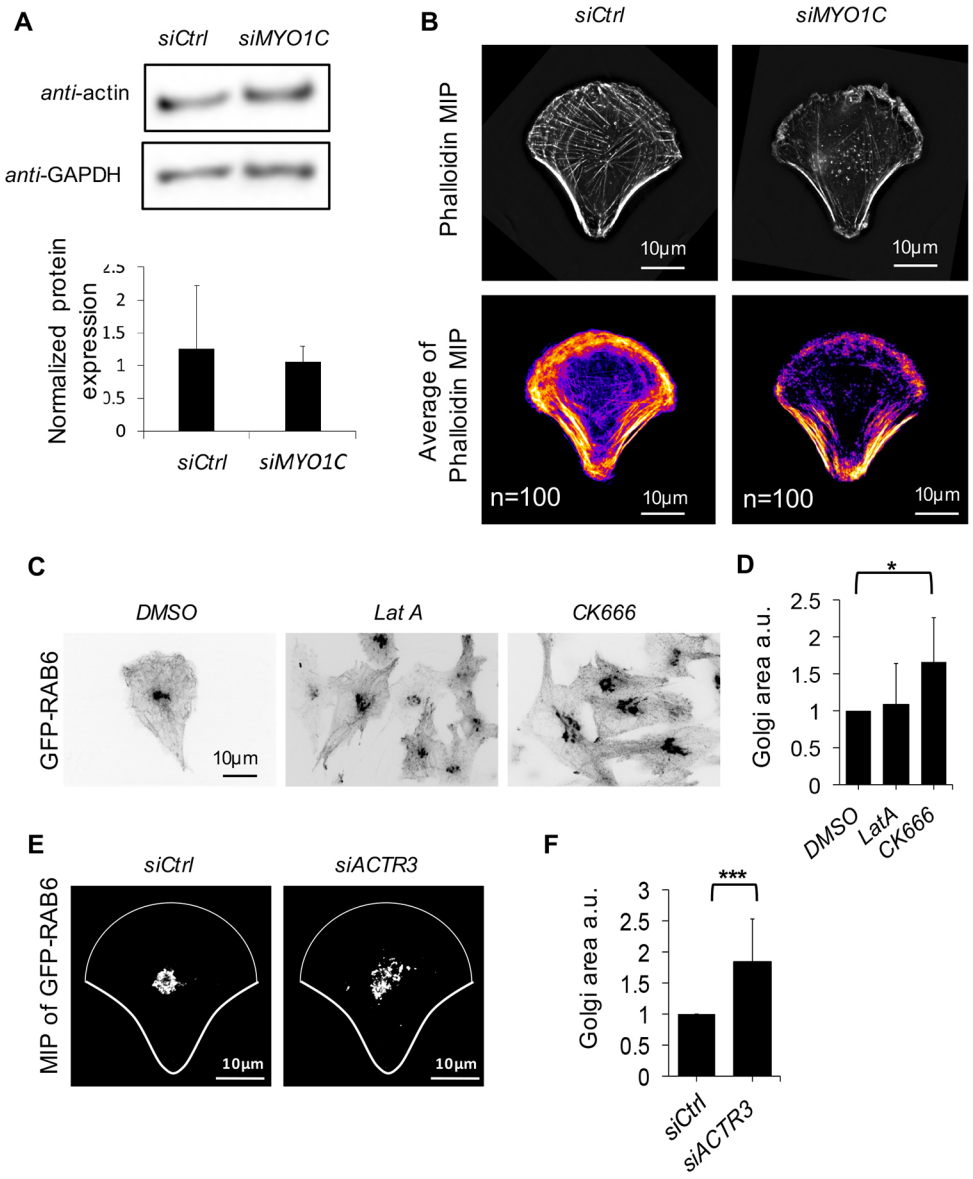

Fig. 6. MYO1C controls cellular actin cytoskeleton. (A) Western blot analysis of actin and GAPDH expression levels in control and MYO1C-depleted hTertRPE-1 cells (top) and densitometry quantification (bottom). Error bars represent the s.d. of three independent experiments. (B) Fluorescent images representing the maximum intensity projections (MIPs) of F-actin stained by phalloidin in representative control and MYO1C-depleted hTertRPE-1 cells seeded on a crossbow-shaped micropattern (top row). Average intensity projection of the MIP images from *n* cells from three independent experiments (bottom row). (C) Fluorescent images of representative, unconstrained hTertRPE-1 cells stably expressing GFP-Rab6 in control conditions and upon treatment with LatA and CK666. (D) Quantification of the 2D projected Golgi area (visualized by GFP-Rab6) in control conditions (n=14) and upon treatment with LatA (n=19) and CK666 (n=15). Error bars represent the s.d. of individual cells. *$P<1\times10^{-2}$, Student's t-test. (E) Fluorescent images representing the MIP of the Golgi complex (visualized by GFP-Rab6) in single, representative hTertRPE-1 cells in control conditions and upon *ACTR3* depletion on a crossbow-shaped micropattern. (F) Quantification of the 2D projected Golgi area (visualized by GFP-Rab6) in control conditions (n=25) and in ACTR3-depleted hTertRPE-1 cells (n=26). Error bars represent the s.d. of individual cells. ***$P<1\times10^{-4}$, Student's t-test. n=number of analyzed cells. Scale bars: 10 µm.

MYO1C delays arrival from anterograde and retrograde trafficking at the Golgi complex

To study the functional consequences of *MYO1C* depletion, we next investigated trafficking through the Golgi complex by live-cell imaging. Employing the retention of different reporter proteins in the ER using selective hooks (RUSH) system (Boncompain and Perez, 2012), we monitored synchronized anterograde transport of GFP-TNFα (also known as TNF) from the ER to the plasma membrane after release of the reporter from the hook. As previously reported, GFP-TNFα accumulated at the Golgi between 10 min and 15 min post-release (Boncompain et al., 2012), which we measured as an increase in the ratio between mean intensity of GFP-TNFα in GM130-positive Golgi area and a random cytosolic area of the same size (Fig. 7A,B). Depletion of *MYO1C* led to a significant delay in the arrival at the Golgi complex at 10 min post-release. In contrast, no difference between control and siMYO1C was detected after 35 min post-release, suggesting that the exit of GFP-TNFα from the Golgi is not delayed upon *MYO1C* depletion, although we cannot exclude that effects on Golgi exit are masked by the different kinetics during Golgi arrival/transit. We additionally analyzed a second cargo, GFP-CD59, for which transport through the Golgi follows slower kinetics than those of TNFα: GFP-CD59 passed the Golgi between 20 min and 45 min post-release. Consistently, we found that depletion of *MYO1C* significantly delayed the arrival of GFP-CD59 at the Golgi, accumulating there only 45 min post-release (Fig. S6A,B). The Golgi complex can receive cargo from the retrograde pathway (Mallard et al., 1998). Thus, we next tested accumulation of Shiga toxin subunit B (STxB) at the Golgi during its trafficking from pre-loaded endosomes to the ER according to standard protocols. STxB accumulated in the Golgi complex starting at 15 min post-release from endosomes, as previously reported. Again, we observed a significant delay in Golgi arrival upon *MYO1C* depletion (Fig. 7C,D) at 15 min and 90 min post-release from endosomes. At 240 min post-release, no differences between control and siMYO1C were detected, indicating that the exit of STxB from the Golgi was not delayed upon *MYO1C* depletion. Thus, MYO1C facilitates the arrival at the Golgi from either anterograde or retrograde routes.

DISCUSSION

Our work identifies MYO1C as a novel trafficking regulator at the Golgi complex. Based on our results we propose that MYO1C localizes in the proximity of the Golgi complex through its PH

Journal of Cell Science (2019) 132, jcs225029. doi:10.1242/jcs.225029

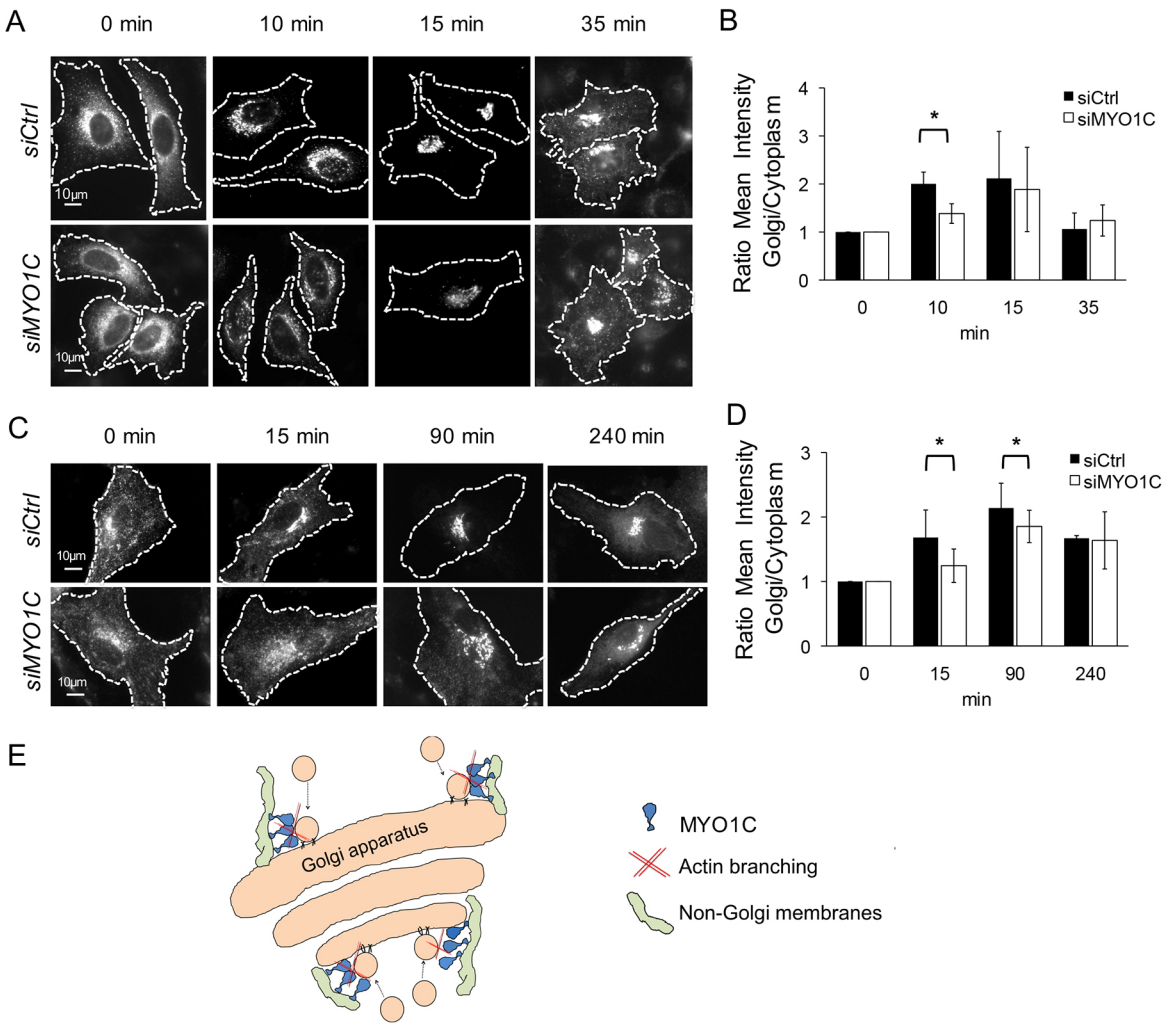

Fig. 7. MYO1C delays arrival from anterograde and retrograde trafficking at the Golgi complex. (A) Fluorescent images of representative, unconstrained hTertRPE-1 cells stably expressing Str–KDEL_TNFα–SBP–GFP at the indicated time points after the release of TNFα–SBP–GFP from the ER in control conditions and in siMYO1C-treated cells. (B) Quantification of the mean fluorescent intensity at the Golgi complex relative to a non-Golgi area of the same size in control conditions (*n* between 63 and 128 for each time point) and upon *MYO1C* depletion (*n* between 55 and 114 for each time point). Error bars represent the s.d. of three independent experiment. **P*<5×10^{-2}, Student's *t*-test, average of three independent experiments. (C) Fluorescent images of representative, unconstrained hTertRPE-1 cells loaded with fluorescently labeled STxB at the indicated time points after release from pre-loaded endosomes in control conditions and in siMYO1C-treated cells. (D) Quantification of the mean fluorescent intensity at the Golgi complex relative to a non-Golgi area of the same size in control conditions (*n* between 40 and 50 for each time point) and upon *MYO1C* depletion (*n* between 40 and 49 for each time point). Error bars represent the s.d. of three independent experiments. **P*<5×10^{-2}, Student's *t*-test. *n*=number of analyzed cells. (E) Model of MYO1C function at the Golgi complex. We propose that MYO1C accumulates in the proximity of the Golgi complex, on non-Golgi membranes, by its PH domain and stabilizes branched actin, facilitating the arrival of incoming transport carriers at the Golgi complex. Dashed lines represent the outlines of cells. Scale bars: 10 µm.

domain, where it stabilizes actin and facilitates the arrival of incoming transport carriers (Fig. 7E). This proposed function of MYO1C differs substantially from those described for other Golgi-associated myosins, which have all been implicated in cargo exit from the Golgi complex. Indeed, myosins are required for the production of tensile forces for deformation of Golgi complex membranes for efficient tubule and vesicle formation and fission. Our work proposes that MYO1C is required for incoming Golgi cargos, organizing a scaffold of actin to facilitate the arrival of cargos at membranes. However, we cannot ascertain that Golgi-associated MYO1C dictates trafficking effects at the Golgi, because MYO1C supports various cellular events, including the cellular distribution of cholesterol-enriched membranes (Brandstaetter et al., 2012). Thus, Golgi complex morphology could be affected by global alterations in the integrity/dynamics of the actin cytoskeleton and/or changes in overall vesicular traffic.

The best-studied function of MYO1C is its role in the docking of GLUT4 (also known as SLC2A4)-containing vesicles to the plasma membrane in response to insulin stimulation (Boguslavsky et al., 2012; Bose et al., 2002, 2004; Chen et al., 2007; Huang et al., 2005; Yip et al., 2008). More generally, MYO1C has been shown to regulate exocytosis in secretory cells: MYO1C has been implicated in the VEGF (also known as VEGFA)-induced delivery of VEGFR2 (also known as KDR) to the cell plasma membrane (Tiwari et al., 2013) and in surfactant exocytosis (Kittelberger et al., 2016). Concomitantly, MYO1C has been localized to cholesterol-rich lipid microdomains at the plasma membrane. However, in addition to this major pool, MYO1C has also been found on recycling endosomes (Brandstaetter et al., 2012). Considering these studies, and our results on the function of MYO1C at the Golgi, these findings indicate that MYO1C function is not limited to a particular organelle or specific membrane, but could more generally regulate the link between different cellular membranes

Journal of Cell Science (2019) 132, jcs225029. doi:10.1242/jcs.225029

and the actin cytoskeleton. More particularly, we speculate that stabilizing branched actin for the arrival of transport carriers could be a general function of MYO1C in intracellular trafficking.

We evidence that *MYO1C* depletion mimics the loss of the Arp2/3 complex at the Golgi complex. This is in agreement with previous surveys that many class I myosins appear to be able to recruit directly or indirectly the Arp2/3 complex (Soldati, 2003). Interestingly, Joensuu et al. (2014) have found that intracellular actin filament arrays are decorated by both MYO1C and cortactin, which is a good marker of branched actin networks in cells (Molinie and Gautreau, 2018). They show that the depletion of *MYO1C* abolished these actin structures and proposed that MYO1C is required for formation of actin filament arrays. Interestingly, it has been shown that manipulation of the expression of another class I myosin, MYO1B, affects the distribution of Arp2/3 and associated branched F-actin (Almeida et al., 2011). MYO1C has been previously shown to alter actin architecture in neuronal growth cones and at the immunological synapse in B cells (Joensuu et al., 2014; Maravillas-Montero et al., 2011). Thus, we propose that MYO1C reorganizes actin architecture. In the future, it will be important to address how MYO1C molecularly stabilizes actin filaments. So far, it is unclear whether myosin I motors influence actin dynamics by direct binding to branching actin filaments, or by recruitment of factors that are involved in nucleation, polymerization and stabilization of actin filaments (McIntosh and Ostap, 2016; McIntosh et al., 2018; Evangelista et al., 2000).

In addition to MYO1C, we have identified MYO6, MYO18 and MYH9 (myosin IIA) as regulators of Golgi complex morphology in our density-based analysis. Although this confirms previous findings, the particular Golgi phenotype (for instance fragmentation, compaction) upon the depletion of a myosin seems to vary and to depend on several factors: (1) cell spreading, which can strongly impact the phenotypes of intracellular organelles; (2) cell type, reflecting variability in actin architectures; or (3) imaging techniques, either visualizing a projected 2D area or the 3D volume of the Golgi complex. For instance, *MYO18A* depletion has been reported to prevent the lateral stretching of the Golgi complex often observed in 2D culture (Dippold et al., 2010). On the other hand, an expansion of the Golgi in the vertical direction as a result of actin filament disassembly downstream of *MYO18A* depletion was proposed by Bruun et al. (2017). Our approach on micropatterns has the advantage that we can detect intracellular changes independently of changes in cell adhesion, and thus allows comparison after the depletion of different myosins in one cell type. Our results indicate that *MYO1C* and *MYO6* depletion de-compacts the Golgi complex, whereas depletion of *MYO18A* and *MYH9* leads to a more compact or smaller Golgi complex, increasing the number of Golgi structures in the case of *MYO18A* silencing and decreasing the Golgi area and number of Golgi structures downstream of *MYH9* depletion. In the future, it will be important to address the difference or redundancy of the functions of myosins, to classify their activities, and to detect potentially synergetic and opposing (tug of war) roles. Quantitative comparative studies under normalized culture conditions are required in the future to comprehensively understand how the different myosins maintain the structural and functional integrity of the Golgi complex.

MATERIALS AND METHODS

Cells and reagents

hTertRPE-1 cells (Invitrogen, Eugene, OR, USA) were grown in Dulbecco's modified Eagle medium (DMEM)/F12 medium (Life Technologies, Carlsbad, CA, USA), supplemented with 10% fetal bovine serum (FBS; Eurobio, Courtaboeuf, France), and 1% penicillin-streptomycin (Life Technologies), in a humidified atmosphere containing 5% CO_2. The RUSH stable cell lines, either expressing Strep-KDEL_CD59–SBP–GFP in hTertRPE-1 cells or Str–KDEL_TNFα–SBP–GFP in HeLa cells, were kindly provided by Frank Perez (Institut Curie, France). The stable HeLa-Kyoto BAC cell lines (human MYO1C-NFLAP, mouse MYO1C-NFLAP) were from the Hyman laboratory (Max Planck Institute of Molecular Cell Biology and Genetics, Dresden, Germany). For micropatterning experiments, fibronectin was from Sigma-Aldrich (St. Louis, MO, USA), fibrinogen–Cy5 from Invitrogen, and poly-L-lysine(20)-grafted[3.5]-polyethyleneglycol(2) (PLL-g-PEG) from SuSoS (Dübendorf, Switzerland). The PLL-g-PEG was used at a final concentration of 0.1 mg/ml in 10 mM HEPES (pH 7.3) solution. We used the following antibodies: mouse monoclonal anti-GM130 (1:1000; BD Biosciences, 610823), anti-MYO1C (1:100; Santa Cruz Biotechnology, sc-136544) and anti-actin (1:5000; Sigma-Aldrich, A-2228); rabbit polyclonal anti-Lamp1 (1:1000; Sigma-Aldrich, L1418 or Abcam, ab24170); human monoclonal anti-tubulin (1:200; F2C-hFc) and anti-Giantin (1:300; Recombinant Protein and Antibody Platform of the Institut Curie); and sheep polyclonal anti-TGN46 (1:500; Bio-Rad, AHP500). FluoProbes 547H (557/572 nm)-coupled phalloidin was from Interchim. Cy3-coupled STxB was generously provided by Ludger Johannes (Institut Curie, Paris, France). Nuclei were stained using 0.2 µg/ml 4′,6-diamidino-2-phenylindole (DAPI; Sigma-Aldrich).

Cell transfection

Cells (200,000) were transfected in either six-well plates or 12-well plates with 25 pmol/ml siRNA (Sigma-Aldrich) using Lipofectamine RNAi MAX Transfection Reagent (5 µl/ml; Life Technologies). Cells were incubated for 72 h prior to further manipulations. MYO1C-siRNA 5′-GCUCAAAGAA-UCCCAUUAU-3′; MYH9-siRNA 5′-GCACAGAGCUGGCCGACAA-3′; MYO18A-siRNA 5′-GGAGAUUAAUGGGCACAAU-3′; MYO6-siRNA 5′-CAAAGUCUGUUACUGAUUA-3′; ACTR3-siRNA 5′-CCGGCTGA-AATTAAGTGAGGA-3′ were used.

Efficiency of siRNA gene silencing was verified by performing real-time PCR on cell mRNA or western blotting on cell lysates after 3 days of transfection. Controls were performed with siRNA targeting Luciferase. DNA transfection was performed using X-tremeGENE9 (Roche) following the manufacturer's instructions. The plasmids used were GFP-MYO1C (from Ana-Maria Lennon, Institut Curie, Paris, France), GFP-MYO1C ΔABL (from Eija Jokitalo, Institute of Biotechnology, University of Helsinki, Helsinki, Finland), MYO1C tail (from Woo Keun Song, Institute of Science and Technology, Gwangju, Korea) and mCherry-Rab6. The siRNA library targeting 36 myosins was kindly provided by Buzz Baum (Rohn et al., 2014).

Screening procedure and analysis

An siRNA library targeting 36 myosin proteins (four siRNAs/gene; 10 nM) was kindly provided by Baum Buzz (University College London, London, UK). For siRNA transfection, hTertRPE-1 cells were seeded on black clear-bottom 96-well plates (Perkin Elmer ViewPlate-96 Black, 6005182) at 70% confluency and transfected using 0.3 µl/well INTERFERin (Polyplus Transfection). Negative siRNA control (Luciferase, GL2) and a positive lethal siRNA (KIF11) were used as transfection controls. After 48 h, decreased cell viability in the lethal positive control wells served as an indicator of successful transfection (beta-factor was over 4 for each individual triplicate). Cells were then dissociated using Accumax™ solution (Sigma-Aldrich) and transferred to micropatterned-printed 96-well plates (CYTOO, Grenoble, France) containing crossbow micropatterns at a concentration of 4000 cells/well. Plates were kept at 37°C for 3 h and further cells were fixed with 4% (w/v) formaldehyde for 15 min and processed for immunofluorescence staining with anti-GM130 primary antibodies. After washing three times with PBS, cells were stained with Cy3 donkey anti-mouse (Interchim, 1/200) in PBS/0.2% bovine serum albumin (BSA)/0.05% saponin for 1 h at 37°C. Nuclei were stained with 0.2 µg/ml DAPI (Sigma-Aldrich). Three independent experiments were performed. Images were acquired using the INCell2000 automated imager (GE Healthcare). Acquisition was performed using a 20× dry objective and 42 fields per well were acquired, giving rise to ∼150 single cells per well. Images were sorted in ImageJ (http://imagej.nih.gov/ij/) using the Micropatterned Single

Cell Sorting (MSCS) plugin, as previously described (Grossier et al., 2014a). Images of single micropatterned cells were segmented with multidimensional image analysis (MIA), and the positional information of the Golgi complex was employed for density-based statistical analysis. Each of the wells containing cells transfected with siRNA against myosins was compared to six control wells on the same plate. The pairwise comparison of endosomal spatial distributions was carried out using the two-sample kernel density-based test (Duong et al., 2012; Schauer et al., 2014). Conditions were considered as hits if average Golgi morphology of a siRNA-treated well was significantly different (P<0.0005) to those of three independent control wells, and reproducible for one specific siRNA in three independent experiments or for two siRNAs in two independent experiments.

Micropatterned coverslip preparation and cell seeding

Micropattern production was as previously described (Azioune et al., 2009) using photo-lithography methods. Briefly, coverslips were coated with PLL-g-PEG and spatially controlled areas were exposed to deep UV light for 5 min using a photomask. Crossbows (37 µm diameter, 7 µm thick) were therefore photo printed. Prior to cell seeding, the patterned substrates were incubated for 1 h with fibronectin at a concentration of 50 µg/ml. The fibronectin mixture was supplemented with 10 µg/ml fibrinogen–Cy5 to stain the micropatterns. Cells were seeded on micropatterns in DMEM/F12 medium supplemented with 10 mM HEPES for 3 h prior to experiments.

Drug treatments

To induce cytoskeleton changes, the following drugs were used at the indicated concentrations for 20 min: 200 nM LatA (Sigma-Aldrich, L5163), 100 µM CK666 (Sigma-Aldrich, SML0006). Dimethyl sulfoxide (DMSO) was used for control conditions.

Immunofluorescence

For immunofluorescence, formaldehyde-fixed cells were washed three times with PBS and permeabilized in PBS/0.2% BSA/0.05% saponin. Cells were then incubated with a primary antibody for 1 h, washed in PBS and incubated with Alexa-Fluor-488- or Cy3-coupled secondary antibodies (Jackson ImmunoResearch). Slices were mounted in Mowiol (Sigma-Aldrich).

Synchronization of protein secretion by RUSH system

Stable cell lines expressing Strep-KDEL_CD59–SBP–GFP (hTertRPE-1 cells) and Str–KDEL_TNFα–SBP–GFP (HeLa cells) were transfected with MYO1C-siRNA or Luciferase-siRNA. After 72 h, cells were treated with 40 µM biotin to allow the reporter release into the secretory pathway. Cells were fixed at the indicated time points after biotin addition, stained with antibody against GM130 and imaged.

STxB assay

hTertRPE-1 cells were transfected with MYO1C-siRNA or Luciferase-siRNA. After 72 h, cells were incubated with Cy3-STxB (1 µg/ml) for 1 h at 19°C to load STxB in early and recycling endosomes, followed by three washes with PBS. Fresh medium was added, and cells were transferred at 37°C for 15, 90 and 240 min, fixed, stained with antibody against GM130 and imaged.

EM

hTertRPE-1 cells were transfected with siRNA-MYO1C or siRNA-LUC for 72 h and chemically fixed with 2% glutaraldehyde and 1% paraformaldehyde in NaHCa buffer (100 mM NaCl, 30 mM HEPES, and 2 mM $CaCl_2$ at pH 7.4). The specimens were post-fixed with 1% OsO4/1.5% $K_4Fe(CN)_6$, dehydrated with a graded ethanol series and embedded in Epon 812 (TAAB Laboratories Equipment). Ultrathin sections were mounted on EM grids, and stained with uranylacetate and lead citrate. Sections were observed with a transmission electron microscope (Tecnai Spirit, Thermo Fisher Scientific, Eindhoven, Netherlands) and digital acquisitions were made with a numeric camera (Quemesa; EMSIS, Münster, Germany).

Single-molecule localization microscopy

Cells were pre-fixed with 0.2% glutaraldehyde/0.25% Triton X-100 in PHEM (60 mM Pipes, 25 mM HEPES, 10 mM EGTA, 4 mM Mg acetate) for 2 min at 37°C and fixed with 2% glutaraldehyde in PHEM for 10 min at 37°C, followed by washes with PBS and aldehyde reduction with NaBH4 (1 mg/ml in PBS) for 10 min. MYO1C was visualized through immunofluorescence using anti-MYO1C (Santa Cruz Biotechnology, sc-136544) primary antibodies and Alexa-Fluor-555-coupled secondary antibodies. Actin was visualized by incubation with phalloidin-Alexa Fluor 647 diluted in PBS/1% BSA for 1 h at 37°C. Samples were mounted in dSTORM buffer (Abbelight, Paris, France). Then, 3D nanoscopy images were taken using a SAFe360 module (Abbelight) coupled to the camera port of an inverted bright-field Olympus IX71 microscope, equipped with a 100× oil-immersion objective with a high numerical aperture (NA; 1.49). This quad-view system (dual-cam sCMOS cameras, Orcaflash v4, Hamamatsu) provided 3D nanoscopy information with high isotropic localization precision (15×15×15 nm, over an axial range of ∼1 mm). Axial information was obtained by super-critical angle fluorescence (SAF) and the point spread function (PSF) deformation with a strong astigmatism (DAISY) (Cabriel et al., 2018). Twenty-thousand frames at 50 ms were acquired to collect the single-molecule detections and reconstruct a nanoscopy image. Resulting coordinate tables and images were processed and analyzed using SAFe NEO software (Abbelight).

Fluorescent image acquisition

For micropatterned cells, Z-stack images from fixed and immunolabeled cells were acquired with an inverted widefield Deltavision Core Microscope (Applied Precision) equipped with a highly sensitive cooled interlined charge coupled device (CCD) camera (CoolSnap Hq2, Photometrics). Z-dimension series were acquired every 0.2 µm and out-of-focus signals were reduced using deconvolution. Non-constrained cells were examined using a 3D deconvolution microscope (Leica DM-RXA2), equipped with a z-drive (Physik Instrument) and 100×/1.4 NA PL-APO objective lens. Then, 3D or 1D multicolor image stacks were acquired using Metamorph software (MDS) through a cooled CCD camera (Photometrics Coolsnap HQ). Z-dimension series were acquired every 0.2 µm. For video microscopy experiments, transfected cells were grown on glass-bottom Fluorodishes. Video microscopy was performed at 37°C using a spinning-disk microscope mounted on an inverted motorized microscope (Nikon TE2000-U) through a 100×/1.4 NA PL-APO objective lens. The microscope was equipped with a Yokogawa CSU-22 spinning-disk head, a Roper Scientific laser launch, a Photometrics Coolsnap HQ2 CCD camera for image acquisition and MDS to control the setup. Z-dimension series were acquired every 0.2 µm.

Image analysis

Golgi area was selected based on GM130 immunostaining and the area and mean intensity were measured in ImageJ. Values were normalized to control conditions (non-transfected, DMSO or siLUC). In anterograde and retrograde transport assays, a small area in the Golgi (GM130 positive) and a random cytoplasmic area of the same size was selected, and mean fluorescent intensities were measured for GFP-TNFα, GFP-CD59 and Cy3-ShTx using ImageJ. Values were expressed as mean intensity ratio of Golgi/cytoplasm. Colocalization analysis was performed with an in-house object-based macro in ImageJ as previously described (Bolte and Cordelieres, 2006; Grossier et al., 2014b). Briefly, two structures were considered colocalized if the distance between their centroids (MIA segmentation output) were found inferior to the optical resolution limit (350 nm in Z-Y, 900 nm in Z). Colocalization results are given as the percentage of colocalized structures over the total number of structures.

Statistical analysis

For each experiment, a large number of cells were monitored from three independent experiments. Data from independent experiments were combined for representation, and statistical analysis was performed employing a bilateral Student's t-test.

Kernel density estimation

To extract the 3D spatial coordinates of intracellular structures, images of several tens of cells were segmented with the MIA interface on MetaMorph (https://www.moleculardevices.com/products/cellular-imaging-systems/acquisition-and-analysis-software/metamorph-microscopy) based on wavelet decomposition. The coordinates from all cells in one condition were aligned

according to the micropattern as previously described (Grossier et al., 2014b; Schauer et al., 2010). The aligned coordinates of the segmented structures were processed for density estimation programmed in the ks library in the R programming language (http://www.r-project.org): the probability density function f for each data sample of n coordinates $X_1, X_2, \ldots, X_n$ was estimated. We used a non-parametric, unbinned kernel density estimator. At each of the data points, a kernel function K was centered. The kernel functions were then summed to form the kernel density estimator $\hat{f}$:

$$\hat{f}_H(x) = \frac{1}{n}\sum_{i=1}^{n} K_H(x - X_i),$$

in which K_H is the Gaussian kernel with mean zero and variance matrix H. To estimate H (also known as the bandwidth), we used the plug-in selector in the ks library that has been shown to be reliable for 2D and 3D spatial distributions. For visualizing kernel density estimates, we used probability contours and the extension libraries mvtnorm, rgl and miscd.

Acknowledgements
We acknowledge the following people for providing materials: Franck Perez, Ana-Maria Lennon-Duménil, Eija Jokitalo, Michael Schell and Woo Keun Song for plasmids; and Buzz Baum for the myosin library. We thank Tarn Duong for advice on statistical analysis and kernel density estimation; Sarah Tessier for the siRNA screening technical assistance; and Patricia Davidson for critical reading of the manuscript. We greatly acknowledge the Cell and Tissue Imaging Facility (PICT-IBiSA, PICT-EM and PICT-IBiSA) and Nikon Imaging Center, Institut Curie (Paris), member of the French National Research Infrastructure France-BioImaging (ANR10-INBS-04).

Competing interests
The authors declare no competing or financial interests.

Author contributions
Conceptualization: A.C., B.G., K.S.; Methodology: A.C., A.Y., V.C., E.D.N., K.S.; Software: K.S.; Validation: K.S.; Formal analysis: A.C., R.K., K.S.; Investigation: A.C., K.S.; Resources: E.C., B.G., K.S.; Data curation: A.C., A.Y., R.K., V.C., A.L., K.S.; Writing - original draft: A.C., K.S.; Writing - review & editing: A.C., E.D.N., E.C., B.G., K.S.; Visualization: A.C., K.S.; Supervision: K.S.; Project administration: A.C., E.C., B.G., K.S.; Funding acquisition: E.C., B.G., K.S.

Funding
This work was supported by Labex CelTisPhyBio [ANR-10-LBX-0038] and Université de Recherche Paris Sciences et Lettres [ANR-10-IDEX-0001-02 PSL], as well as grants from Agence Nationale de la Recherche [#2010 BLAN 122902], the European Research Council [project 339847 'MYODYN'], Centre National de la Recherche Scientifique and Institut Curie.

Supplementary information
Supplementary information available online at
http://jcs.biologists.org/lookup/doi/10.1242/jcs.225029.supplemental

References
Almeida, C. G., Yamada, A., Tenza, D., Louvard, D., Raposo, G. and Coudrier, E. (2011). Myosin 1b promotes the formation of post-Golgi carriers by regulating actin assembly and membrane remodelling at the trans -Golgi network. *Nat. Cell Biol.* **13**, 779-789. doi:10.1038/ncb2262

Azioune, A., Storch, M., Bornens, M., Théry, M. and Piel, M. (2009). Simple and rapid process for single cell micro-patterning. *Lab. Chip* **9**, 1640-1642. doi:10.1039/b821581m

Boguslavsky, S., Chiu, T., Foley, K. P., Osorio-Fuentealba, C., Antonescu, C. N., Bayer, K. U., Bilan, P. J. and Klip, A. (2012). Myo1c binding to submembrane actin mediates insulin-induced tethering of GLUT4 vesicles. *Mol. Biol. Cell* **23**, 4065-4078. doi:10.1091/mbc.e12-04-0263

Bolte, S. and Cordelieres, F. P. (2006). A guided tour into subcellular colocalization analysis in light microscopy. *J. Microsc.* **224**, 213-232. doi:10.1111/j.1365-2818.2006.01706.x

Boncompain, G., Divoux, S., Gareil, N., de Forges, H., Lescure, A., Latreche, L., Mercanti, V., Jollivet, F., Raposo, G. and Perez, F. (2012). Synchronization of secretory protein traffic in populations of cells. *Nat Methods* **9**, 493-498. doi:10.1038/nmeth.1928

Bose, A., Guilherme, A., Robida, S. I., Nicoloro, S. M. C., Zhou, Q. L., Jiang, Z. Y., Pomerleau, D. P. and Czech, M. P. (2002). Glucose transporter recycling in response to insulin is facilitated by myosin Myo1c. *Nature* **420**, 821-824. doi:10.1038/nature01246

Bose, A., Robida, S., Furcinitti, P. S., Chawla, A., Fogarty, K., Corvera, S. and Czech, M. P. (2004). Unconventional myosin Myo1c promotes membrane fusion in a regulated exocytic pathway. *Mol. Cell. Biol.* **24**, 5447-5458. doi:10.1128/MCB.24.12.5447-5458.2004

Brandstaetter, H., Kendrick-Jones, J. and Buss, F. (2012). Myo1c regulates lipid raft recycling to control cell spreading, migration and Salmonella invasion. *J. Cell Sci.* **125**, 1991-2003. doi: 10.1242/jcs.097212

Bruun, K., Beach, J. R., Heissler, S. M., Remmert, K., Sellers, J. R. and Hammer, J. A. (2017). Re-evaluating the roles of myosin 18Aα and F-actin in determining Golgi morphology. *Cytoskeleton* **74**, 205-218. doi:10.1002/cm.21364

Cabriel, C., Bourg, N., Dupuis, G. and Lévêque-Fort, S. (2018). Aberration-accounting calibration for 3D single-molecule localization microscopy. *Opt. Lett.* **43**, 174-177. doi:10.1364/OL.43.000174

Chen, X.-W., Leto, D., Chiang, S.-H., Wang, Q. and Saltiel, A. R. (2007). Activation of RalA is required for insulin-stimulated glut4 trafficking to the plasma membrane via the exocyst and the motor protein myo1c. *Dev. Cell* **13**, 391-404. doi:10.1016/j.devcel.2007.07.007

Dippold, H. C., Ng, M. M., Farber-katz, S. E., Lee, S., Monica, L., Peterman, M. C., Sim, R., Wiharto, P. A., Galbraith, K. A., Madhavarapu, S. et al. (2010). GOLPH3 bridges phosphatidylinositol-4- phosphate and actomyosin to stretch and shape the Golgi to promote budding. *Cell* **139**, 337-351. doi:10.1016/j.cell.2009.07.052

Duong, T., Goud, B. and Schauer, K. (2012). Closed-form density-based framework for automatic detection of cellular morphology changes. *Proc. Natl Acad. Sci. USA* **109**, 8382-8387. doi:10.1073/pnas.1117796109

Evangelista, M., Klebl, B. M., Tong, A. H. Y., Webb, B. A., Leeuw, T., Leberer, E., Whiteway, M., Thomas, D. Y. and Boone, C. (2000). A role for myosin-I in actin assembly through interactions with Vrp1p, Bee1p, and the Arp2/3 complex. *J. Cell Biol.* **148**, 353-362. doi:10.1083/jcb.148.2.353

Goud, B., Liu, S. and Storrie, B. (2018). Rab proteins as major determinants of the Golgi complex structure. *Small GTPases* **9**, 66-75. doi:10.1080/21541248.2017.1384087

Grossier, J. P., Goud, B. and Schauer, K. (2014a). Probabilistic density maps to study the spatial organization of endocytosis. *Methods Mol. Biol.* **1174**, 117-138. doi:10.1007/978-1-4939-0944-5_8

Grossier, J. P., Xouri, G., Goud, B. and Schauer, K. (2014b). Cell adhesion defines the topology of endocytosis and signaling. *EMBO J.* **33**, 35-45. doi:10.1002/embj.201385284

Hokanson, D. E., Laakso, J. M., Lin, T., Sept, D. and Ostap, E. M. (2006). Myo1c binds phosphoinositides through a putative pleckstrin homology domain. *Mol. Biol. Cell* **17**, 4856-4865. doi:10.1091/mbc.e06-05-0449

Huang, J., Imamura, T., Babendure, J. L., Lu, J. C. and Olefsky, J. M. (2005). Disruption of microtubules ablates the specificity of insulin signaling to GLUT4 translocation in 3T3-L1 adipocytes. *J. Biol. Chem.* **280**, 42300-42306. doi:10.1074/jbc.M510920200

Joensuu, M., Belevich, I., Ramo, O., Nevzorov, I., Vihinen, H., Puhka, M., Witkos, T. M., Lowe, M., Vartiainen, M. K. and Jokitalo, E. (2014). ER sheet persistence is coupled to myosin 1c-regulated dynamic actin filament arrays. *Mol. Biol. Cell* **25**, 1111-1126. doi:10.1091/mbc.e13-12-0712

Johnson, H. W. and Schell, M. J. (2009). Neuronal IP3 3-kinase is an F-actin-bundling protein: role in dendritic targeting and regulation of spine morphology. *Mol. Biol. Cell* **20**, 5166-5180. doi:10.1091/mbc.e09-01-0083

Kittelberger, N., Breunig, M., Martin, R., Knölker, H.-J. and Miklavc, P. (2016). The role of myosin 1c and myosin 1b in surfactant exocytosis. *J. Cell Sci.* **129**, 1685-1696. doi:10.1242/jcs.181313

Liu, Y., Xu, X.-H., Chen, Q., Wang, T., Deng, C.-Y., Song, B.-L., Du, J.-L. and Luo, Z.-G. (2013). Myosin Vb controls biogenesis of post-Golgi Rab10 carriers during axon development. *Nat. Commun.* **4**, 2005. doi:10.1038/ncomms3005

Maliga, Z., Junqueira, M., Toyoda, Y., Ettinger, A., Mora-Bermúdez, F., Klemm, R. W., Vasilj, A., Guhr, E., Ibarlucea-Benitez, I., Poser, I. et al. (2013). A genomic toolkit to investigate kinesin and myosin motor function in cells. *Nat. Cell Biol.* **15**, 325-334. doi:10.1038/ncb2689

Mallard, F., Antony, C., Tenza, D., Salamero, J., Goud, B. and Johannes, L. (1998). Direct pathway from early/recycling endosomes to the Golgi apparatus revealed through the study of Shiga toxin B-fragment transport. *J. Cell Biol.* **143**, 973-990. doi:10.1083/jcb.143.4.973

Maravillas-Montero, J. L., Gillespie, P. G., Patino-Lopez, G., Shaw, S. and Santos-Argumedo, L. (2011). Myosin 1c participates in B cell cytoskeleton rearrangements, is recruited to the immunologic synapse, and contributes to antigen presentation. *J. Immunol.* **187**, 3053-3063. doi:10.4049/jimmunol.1004018

McIntosh, B. B. and Ostap, E. M. (2016). Myosin-I molecular motors at a glance. *J. Cell Sci.* **129**, 2689-2695. doi:10.1242/jcs.186403

McIntosh, B. B., Pyrpassopoulos, S., Holzbaur, E. L. F. and Ostap, E. M. (2018). Opposing kinesin and myosin-i motors drive membrane deformation and tubulation along engineered cytoskeletal networks. *Curr. Biol.* **28**, 236-248.e5. doi:10.1016/j.cub.2017.12.007

Miserey-Lenkei, S., Chalancon, G., Bardin, S., Formstecher, E., Goud, B. and Echard, A. (2010). Rab and actomyosin-dependent fission of transport vesicles at the golgi complex. *Nat. Cell Biol.* **12**, 645-654. doi:10.1038/ncb2067

Molinie, N. and Gautreau, A. (2018). The Arp2/3 regulatory system and its deregulation in cancer. *Physiol. Rev.* **98**, 215-238. doi:10.1152/physrev.00006.2017

Müsch, A., Cohen, D. and Rodriguez-Boulan, E. (1997). Myosin II is involved in the production of constitutive transport vesicle from the TGN. *J. Cell Biol.* **138**, 291-306. doi:10.1083/jcb.138.2.291

Oh, H., Kim, H., Shin, B., Lee, K. H., Yeo, M. G. and Song, W. K. (2013). Interaction of Crk with myosin-1c participates in fibronectin-induced cell spreading. *Int. J. Biol. Sci.* **9**, 778-791. doi:10.7150/ijbs.6459

Pyrpassopoulos, S., Feeser, E. A., Mazerik, J. N., Tyska, M. J. and Ostap, E. M. (2012). Membrane-bound Myo1c powers asymmetric motility of actin filaments. *Curr. Biol.* **22**, 1688-1692. doi:10.1016/j.cub.2012.06.069

Rohn, J. L., Patel, J. V., Neumann, B., Bulkescher, J., McHedlishvili, N., McMullan, R. C., Quintero, O. A., Ellenberg, J. and Baum, B. (2014). Myo19 ensures symmetric partitioning of mitochondria and coupling of mitochondrial segregation to cell division. *Curr. Biol.* **24**, 2598-2605. doi:10.1016/j.cub.2014.09.045

Ruppert, C., Godel, J., Müller, R. T., Kroschewski, R., Reinhard, J. and Bähler, M. (1995). Localization of the rat myosin I molecules myr 1 and myr 2 and in vivo targeting of their tail domains. *J. Cell Sci.* **108**, 3775-3786.

Schauer, K., Duong, T., Bleakley, K., Bardin, S., Bornens, M. and Goud, B. (2010). Probabilistic density maps to study global endomembrane organization. *Nat. Methods* **7**, 560-566. doi:10.1038/nmeth.1462

Schauer, K., Grossier, J. P., Duong, T., Chapuis, V., Degot, S., Lescure, A., Del Nery, E. and Goud, B. (2014). A novel organelle map framework for high-content cell morphology analysis in high throughput. *J. Biomol. Screen.* **19**, 317-324. doi:10.1177/1087057113497399

Soldati, T. (2003). Unconventional myosins, actin dynamics and endocytosis: a ménage à trois? *Traffic* **4**, 358-366. doi:10.1034/j.1600-0854.2003.t01-1-00095.x

Tang, N. and Ostap, E. M. (2001). Motor domain-dependent localization of myo1b (myr-1). *Curr. Biol.* **11**, 1131-1135. doi:10.1016/S0960-9822(01)00320-7

Tiwari, A., Jung, J.-J., Inamdar, S. M., Nihalani, D. and Choudhury, A. (2013). The myosin motor Myo1c is required for VEGFR2 delivery to the cell surface and for angiogenic signaling. *Am. J. Physiol. Heart Circ. Physiol.* **304**, H687-H696. doi:10.1152/ajpheart.00744.2012

Warner, C. L., Stewart, A., Luzio, J. P., Steel, K. P., Libby, R. T., Kendrick-Jones, J. and Buss, F. (2003). Loss of myosin VI reduces secretion and the size of the Golgi in fibroblasts from Snell's waltzer mice. *EMBO J.* **22**, 569-579. doi:10.1093/emboj/cdg055

Yip, M. F., Ramm, G., Larance, M., Hoehn, K. L., Wagner, M. C., Guilhaus, M. and James, D. E. (2008). CaMKII-mediated phosphorylation of the myosin motor myo1c is required for insulin-stimulated glut4 translocation in adipocytes. *Cell Metab.* **8**, 384-398. doi:10.1016/j.cmet.2008.09.011